

Nine New Metal-Poor Stars on the Subgiant and Red Horizontal Branches with High Levels of r -process Enhancement^{*}

Ian U. Roederer,^{1†} John J. Cowan,² George W. Preston,³
 Stephen A. Shtetman,³ Christopher Sneden,⁴ Ian B. Thompson³

¹*Department of Astronomy, University of Michigan, 1085 S. University Ave., Ann Arbor, MI 48109, USA*

²*Homer L. Dodge Department of Physics and Astronomy, University of Oklahoma, 440 W. Brooks St., Norman, OK 73019, USA*

³*Carnegie Observatories, 813 Santa Barbara St., Pasadena, CA 91101, USA*

⁴*Department of Astronomy, University of Texas at Austin, 1 University Station C1400, Austin, TX 78712, USA*

8 November 2021

ABSTRACT

We report the discovery of nine metal-poor stars with high levels of r -process enhancement ($+0.81 \leq [\text{Eu}/\text{Fe}] \leq +1.13$), including six subgiants and three stars on the red horizontal branch. We also analyze four previously-known r -process-enhanced metal-poor red giants. From this sample of 13 stars, we draw the following conclusions. (1) High levels of r -process enhancement are found in a broad range of stellar evolutionary states, reaffirming that this phenomenon is not associated with a chemical peculiarity of red giant atmospheres. (2) Only 1 of 10 stars observed at multiple epochs shows radial velocity variations, reaffirming that stars with high levels of r -process enhancement are not preferentially found among binaries. (3) Only 2 of the 13 stars are highly-enhanced in C and N, indicating that there is no connection between high levels of r -process enhancement and high levels of C and N. (4) The dispersions in $[\text{Sr}/\text{Ba}]$ and $[\text{Sr}/\text{Eu}]$ are larger than the dispersions in $[\text{Ba}/\text{Eu}]$ and $[\text{Yb}/\text{Eu}]$, suggesting that the elements below the second r -process peak do not always scale with those in the rare earth domain, even within the class of highly- r -process-enhanced stars. (5) The light-element ($12 \leq Z \leq 30$) abundances of highly- r -process-enhanced stars are indistinguishable from those with normal levels of r -process material at the limit of our data, 3.5 per cent (0.015 dex) on average. The nucleosynthetic sites responsible for the large r -process enhancements did not produce any detectable light-element abundance signatures distinct from normal core-collapse supernovae.

Key words: nuclear reactions, nucleosynthesis, abundances — stars: abundances — stars: atmospheres — stars: Population II —

1 INTRODUCTION

Elements heavier than the iron group comprise a minuscule fraction of all atoms by number or mass, but they comprise approximately 70 per cent of the stable or long-lived isotopes found naturally on earth. The rapid neutron-capture process, also known as the r -process, is one of the two general nucleosynthesis mechanisms responsible for production of most isotopes heavier than the iron group (Burbidge et al. 1957). Two decades ago, observations of

the metal-poor star CS 22892–052 ($[\text{Fe}/\text{H}] = -3.1$) revealed a surprising consistency between its heavy-element abundance pattern and the predicted r -process component of the solar system distribution (Sneden et al. 1994; Cowan et al. 1995). Over the next decade, three other stars were found with similar abundance patterns (HD 115444, Westin et al. 2000; CS 31082–001, Hill et al. 2002; and BD+17 3248, Cowan et al. 2002), and since then tens more have been identified (e.g., Barklem et al. 2005). The ratios of heavy elements to Fe (e.g., $[\text{Eu}/\text{Fe}]$) in many of these stars are an order of magnitude larger than in the solar system, and this is one of two defining characteristics of the “ r -II” class of stars (Beers & Christlieb 2005). (The other defining characteristic is that the star has $[\text{Ba}/\text{Eu}] < 0$.) The existence

^{*} This paper includes data gathered with the 6.5 meter Magellan Telescopes located at Las Campanas Observatory, Chile.

[†] E-mail: iur@umich.edu

of this r -process pattern in metal-poor stars nearly as old as the Universe itself was not predicted by theory, and the stellar sites responsible for r -process nucleosynthesis are still debated today.

Our use of the phrase *r-process nucleosynthesis* refers to the generic process described by Burbidge et al. (1957): “a large flux of neutrons becomes available in a short time interval for addition to elements of the iron group” (p. 587). That which produces the predicted r -process abundance pattern in solar system material is the so-called *main component* of the r -process. This is what Burbidge et al. were trying to reproduce with their analytic description, even though it would be another 16 years before others would attempt to separate the r -process contribution explicitly from the slow neutron-capture (s -process) contribution in the solar system total isotopic distribution (Cameron 1973).

The Burbidge et al. definition is, however, sufficiently flexible to account for the “incomplete r -process synthesis” (Truran et al. 2002, p. 1305) abundance pattern, or so-called *weak component*, found in many other metal-poor stars and exemplified by HD 122563 (e.g., Wallerstein et al. 1963; Sneden & Parthasarathy 1983; Honda et al. 2006). The patterns typical of the main and weak components may represent the extremes of a range of r -process nucleosynthesis outcomes that depend on the physical conditions at the time of nucleosynthesis. They may also represent two distinct processes (Montes et al. 2007).

Abundance patterns intermediate between these two extremes are found, and the full range spans at least $-0.5 \leq [\text{Eu}/\text{Fe}] \leq +1.9$ (e.g., Sneden, Cowan, & Gallino 2008). This can be illustrated, for example, with the $[\text{Sr}/\text{Ba}]$ ratio in ≈ 100 stars as shown in in Figure 17 of Cohen et al. (2013). Alternatively, the same effect is shown for many elements in 16 stars in Figure 11 of Roederer et al. (2010). François et al. (2007) and Siqueira-Mello et al. (2014) also find these intermediate values in their samples of metal-poor stars with various levels of r -process enhancement (see their Figures 15 and 28, respectively). Phenomenological chemical evolution models (e.g., Qian & Wasserburg 2008; Aoki et al. 2013) and physically-motivated r -process calculations (e.g., Kratz et al. 2007; Boyd et al. 2012) can reproduce the observed distributions. These explanations, however, are not uniquely capable of predicting the range of $[\text{Sr}/\text{Ba}]$ ratios in low metallicity stars (e.g., Cescutti et al. 2013).

In the literature, references to *the r-process* frequently refer to the event producing the main component pattern. Observations indicating that the r -process is a rare event and those indicating the nearly-ubiquitous presence of r -process material in stars are not mutually exclusive. Abundance patterns like that found in the star CS 22892–052 are rare, and so presumably the nucleosynthesis events that produce them are also rare. The greater concentration of stars with $[\text{Ba}/\text{Fe}]$ and $[\text{Ba}/\text{Sr}] < 0$ and low $[\text{C}/\text{Fe}]$ ratios in Figure 7 of Sneden et al. (2008) indicates that stars with these characteristics, like HD 122563, are not rare (cf. Roederer 2013). Thus the r -process events that give rise to these patterns are probably not rare, either.

In this paper we present nine new members of the class of stars highly-enhanced in r -process material. Until recent years the members of this class included only evolved red giants, as summarized by Cowan et al. (2011). This understandably led to concern that perhaps the consistent

r -process pattern observed in some metal-poor stars was an artifact of the analysis or related to physics of the stellar photospheres rather than nucleosynthesis. The one exception is a faint main sequence dwarf identified by Aoki et al. (2010). The nine stars presented here are subgiants (including stars at the main-sequence turn-off, MSTO) and the field-star equivalents of red horizontal branch (RHB) stars. These stars have been identified among the metal-poor candidates presented by Beers, Preston, & Shtetman (1992) and analyzed in detail by Roederer et al. (2014a).

The details of sample selection, observations, and a summary of the analysis techniques are presented in Sections 2, 3, and 4. We examine these stars for evidence of radial velocity variations in Section 5. Section 6 demonstrates the close matches between the abundance patterns in these stars and four previously-known highly- r -process-enhanced giants, including CS 22892–052. Sections 7, 8, and 9 discuss our results, and Section 10 summarizes our findings.

Throughout this work we adopt the standard definitions of elemental abundances and ratios. For element X, the logarithmic abundance is defined as the number of atoms of X per 10^{12} hydrogen atoms, $\log \epsilon(\text{X}) \equiv \log_{10}(N_{\text{X}}/N_{\text{H}}) + 12.0$. For elements X and Y, the logarithmic abundance ratio relative to the solar ratio, denoted $[\text{X}/\text{Y}]$, is defined as $\log_{10}(N_{\text{X}}/N_{\text{Y}}) - \log_{10}(N_{\text{X}}/N_{\text{Y}})_{\odot}$. We adopt the solar abundances given by Asplund et al. (2009) and listed in Table 13 of Roederer et al. (2014a). Abundances or ratios denoted with the ionization state indicate the total elemental abundance as derived from transitions of that particular state after ionization corrections have been applied. Abundance ratios for elements X and Y compare the total abundances of X and Y derived from like ionization states; i.e., neutrals with neutrals and ions with ions.

2 SAMPLE SELECTION

We draw our sample from the catalog of 313 metal-poor stars observed and analyzed by Roederer et al. (2014a). We adopt a traditional indicator of r -process enrichment to select stars highly-enhanced in r -process material, the $[\text{Eu}/\text{Fe}]$ ratio. The Roederer et al. study included four red giants previously identified as being highly-enhanced in r -process material, CS 22183–031, CS 22892–052, CS 22953–003, and CS 31082–001. Prior studies have generally confirmed that $[\text{Eu}/\text{Fe}] > +1.0$ in each of these stars. As discussed in Section 4, the Roederer et al. $[\text{Eu}/\text{Fe}]$ ratios are lower than those found by previous studies of these four stars by an average of 0.22 dex ($\sigma = 0.10$). Therefore, to remain consistent with the r -II classification scheme, we consider stars with $[\text{Eu}/\text{Fe}] \gtrsim +0.8$ as candidates for inclusion in this class.

Figure 1 illustrates the $[\text{Eu}/\text{Fe}]$ ratios for all stars in the Roederer et al. (2014a) sample. The red line marks $[\text{Eu}/\text{Fe}] = +0.78$. Eu II lines are detected in 15 stars whose $[\text{Eu}/\text{Fe}]$ ratios exceed this limit. Four of these stars are the previously-known giants mentioned above. As we discuss in Section 6, nine of the remaining Eu-rich stars have abundance patterns consistent with that found in previously-identified highly- r -process-enhanced stars and the calculated solar r -process abundance pattern. These stars are marked with large red circles in Figure 1. These nine stars include six sub-

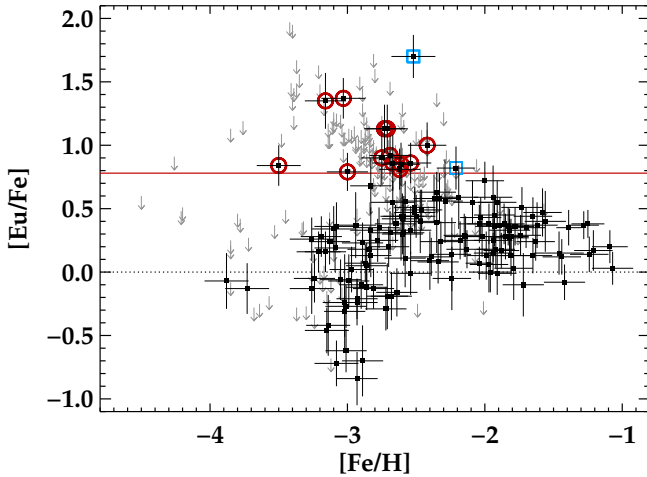


Figure 1. $[\text{Eu}/\text{Fe}]$ ratios for all stars in the Roederer et al. (2014a) sample. The red line marks $[\text{Eu}/\text{Fe}] = +0.78$, the lower limit for classifying a star as highly-enhanced in *r*-process material. Red circles mark stars examined in our study, and the blue squares mark stars with high levels of $[\text{Eu}/\text{Fe}]$ resulting from *s*-process enrichment. The dotted line marks the solar ratio.

giants (CS 22886–012, CS 22943–132, CS 22945–017, CS 22945–058, CS 22958–052, CS 29529–054) and three field stars that occupy the same region of the temperature-gravity diagram as the RHB stars in globular clusters (CS 22875–029, CS 22882–001, CS 22888–047). Preston et al. (2006) presented abundances for a limited selection of heavy elements in these three RHB stars. Their results are similar to those presented here (Section 4), but that study did not discuss the high levels of *r*-process enhancement found in these stars.

Portions of the spectra of the 13 highly-*r*-process-enhanced stars are shown in Figures 2–4. The *n*-capture absorption lines are substantially stronger in the cool giants, and there are many lines present. This illustrates why highly-*r*-process-enhanced stars have been preferentially identified among cool giants. Absorption lines that are weak in cool giants would be swamped by the continuous opacity in warmer stars, rendering them undetectable. None of these subgiants or RHB stars were selected for observation based on the strength of their *n*-capture absorption lines.

Two other stars have $[\text{Eu}/\text{Fe}]$ ratios in excess of the lower limit established to identify highly-*r*-process-enhanced stars (CS 22956–102 and CS 29497–030). Their abundance patterns are clearly indicative of enrichment by large amounts of material produced by *s*-process nucleosynthesis. These stars are marked with blue squares in Figure 1 and discussed separately in the Appendix. We shall not consider them further here.

3 SUMMARY OF OBSERVATIONS AND ANALYSIS TECHNIQUES

Table 1 presents a record of observations. Observations were made with the Magellan Inamori Kyocera Echelle (MIKE) spectrograph (Bernstein et al. 2003) on the 6.5 m Walter Baade and Landon Clay Telescopes (Magellan I and II)

at Las Campanas Observatory. These spectra were taken with the $0''.7 \times 5''.0$ slit, yielding a resolving power of $R \equiv \lambda/\Delta\lambda \sim 41,000$ in the blue and $R \sim 35,000$ in the red as measured from isolated ThAr lines in the comparison lamp images. The red and blue arms are split by a dichroic at $\approx 4950 \text{ \AA}$. This setup achieves complete wavelength coverage from 3350–9150 \AA . Signal to noise (S/N) estimates at several reference wavelengths are listed in Table 2. The footnotes to Table 2 identify stars that were reimaged during the course of the Las Campanas Objective-Prism Survey (Beers et al. 1992) or the Hamburg-ESO Survey (Christlieb et al. 2008).

Roederer et al. (2014a) used model atmospheres interpolated from the grid of one-dimensional MARCS models (Gustafsson et al. 2008) and performed the analysis using a recent version of the spectral line analysis code MOOG (Snedden 1973; see discussion in Sobek et al. 2011). Effective temperatures (T_{eff}) and microturbulent velocities (v_t) were derived by requiring that abundances derived from Fe I lines showed no trend with the excitation potential and line strength. For stars on the horizontal branch, $\log g$ was derived by requiring that the Fe abundance derived from Fe I lines matched that derived from Fe II lines. For the other stars, surface gravities ($\log g$, in cgs units) were calculated from the relationship between T_{eff} and $\log g$ given by theoretical isochrones in the Y^2 grid (Demarque et al. 2004) assuming an age of 12 ± 1.5 Gyr. The Fe abundance derived from Fe II lines was taken to represent the overall metallicity, $[\text{M}/\text{H}]$. The derived model parameters and their statistical (internal) uncertainties are presented in Table 3. These values are identical to those presented in Table 7 of Roederer et al. and are reproduced here for convenience. Roederer et al. estimated the systematic uncertainties by comparing model parameters with those derived in previous studies. For red giants, subgiants, and stars on the horizontal branch, these comparisons for the full sample yielded standard deviations of 151, 211, and 156 K in T_{eff} , 0.40, 0.34, and 0.42 in $\log g$, 0.41, 0.33, and 0.26 km s^{-1} in v_t , and 0.24, 0.22, and 0.16 dex in $[\text{Fe II}/\text{H}]$. We adopt these as the systematic uncertainties in the model atmosphere parameters.

Table 8 of Roederer et al. (2014a) lists the atomic data for each transition studied. Spectrum synthesis was performed for lines broadened by hyperfine splitting or in cases where a significant isotope shift may be present. For unblended lines, Roederer et al. used MOOG to compute theoretical equivalent widths, which were then forced to match measured equivalent widths by adjusting the abundance. Roederer et al. derived 3σ upper limits when a line was not detected. Table 11 of Roederer et al. lists the abundances derived from each line in each star. That study also adopted corrections to account for departures from local thermodynamic equilibrium (LTE) in the line formation regions for Li I (Lind, Asplund, & Barklem 2009), O I (Fabbian et al. 2009), Na I (Lind et al. 2011), and K I (Takeda et al. 2002). Weighted mean abundances and uncertainties were computed using the formalism presented in McWilliam et al. (1995b). We do not repeat the full set of abundances here, but a few key element ratios are reproduced in Table 3 for convenience.

Table 1. Log of Observations

Star	Telescope/ instrument	Exposure length (s)	Date	UT at mid-exposure	Heliocentric Julian date	Heliocentric radial velocity (km s ⁻¹)
Previously-known <i>r</i> -process enhanced stars on the red giant branch						
CS 22183–031	Magellan-Clay/MIKE	1400	2006 Aug 03	10:23	2453950.935	+23.1
CS 22892–052	Magellan-Baade/MIKE	2400	2003 Jun 26	10:12	2452816.928	+12.9
	Magellan-Clay/MIKE	2400	2004 Jun 29	09:11	2453185.886	+13.0
CS 22953–003	Magellan-Clay/MIKE	2000	2006 Aug 03	09:46	2453950.910	+208.3
CS 31082–001	Magellan-Clay/MIKE	1800	2003 Jul 19	10:27	2452839.937	+138.9
New <i>r</i> -process enhanced stars on the subgiant branch or MSTO						
CS 22886–012	Magellan-Clay/MIKE	3600	2008 Sep 12	02:59	2454721.630	–56.8
	Magellan-Clay/MIKE	1800	2009 Sep 05	03:08	2455079.636	–57.0
CS 22943–132	Magellan-Clay/MIKE	1400	2006 Aug 03	02:19	2453950.602	+18.9
CS 22945–017	Magellan-Clay/MIKE	3400	2008 Sep 11	02:58	2454720.627	+101.8
CS 22945–058	Magellan-Clay/MIKE	5400	2008 Sep 11	04:28	2454720.689	+23.1
	Magellan-Clay/MIKE	1550	2009 Jul 26	10:29	2455038.940	+23.7
CS 22958–052	Magellan-Clay/MIKE	3000	2004 Sep 26	09:12	2453274.886	+88.9
CS 29529–054	Magellan-Baade/MIKE	3600	2003 Jan 17	03:27	2452656.643	+113.3
	Magellan-Baade/MIKE	6000	2003 Jan 20	01:08	2452659.547	+112.9
	Magellan-Clay/MIKE	1900	2009 Sep 05	09:59	2455079.917	+113.4
New <i>r</i> -process enhanced stars on the red horizontal branch						
CS 22875–029	Magellan-Baade/MIKE	3600	2003 Jun 12	09:59	2452802.918	+73.1
	Magellan-Clay/MIKE	3600	2003 Oct 12	04:25	2452924.687	+72.7
CS 22882–001	Magellan-Baade/MIKE	4800	2003 Jun 15	09:24	2452805.892	+26.9
	Magellan-Clay/MIKE	6000	2003 Oct 09	06:05	2452921.758	+26.1
CS 22888–047	Magellan-Baade/MIKE	4400	2003 Jun 14	09:00	2452804.876	–158.5
	Magellan-Clay/MIKE	6000	2003 Oct 13	05:15	2452925.723	–158.1

Table 2. Total Exposure Times and S/N Ratios

Star	Total exp. time (s)	No. obs.	S/N 3950 Å	S/N 4550 Å	S/N 5200 Å	S/N 6750 Å
Previously-known <i>r</i> -process enhanced stars on the red giant branch						
CS 22183–031	1400	1	75	105	75	105
CS 22892–052 ^a	4800	2	150	225	175	270
CS 22953–003	2000	1	65	95	75	100
CS 31082–001	1800	1	125	145	230	350
New <i>r</i> -process enhanced stars on the subgiant branch						
CS 22886–012 ^b	5400	2	60	85	80	130
CS 22943–132	1400	1	75	105	75	95
CS 22945–017	3400	1	60	75	75	115
CS 22945–058	6950	2	60	85	80	125
CS 22958–052	3000	1	80	105	55	75
CS 29529–054	11500	3	60	100	110	155
New <i>r</i> -process enhanced stars on the red horizontal branch						
CS 22875–029	7200	2	110	115	160	220
CS 22882–001	10800	2	85	95	120	170
CS 22888–047	10400	2	95	105	150	205

^a HE 2214–1654^b CS 29512–015

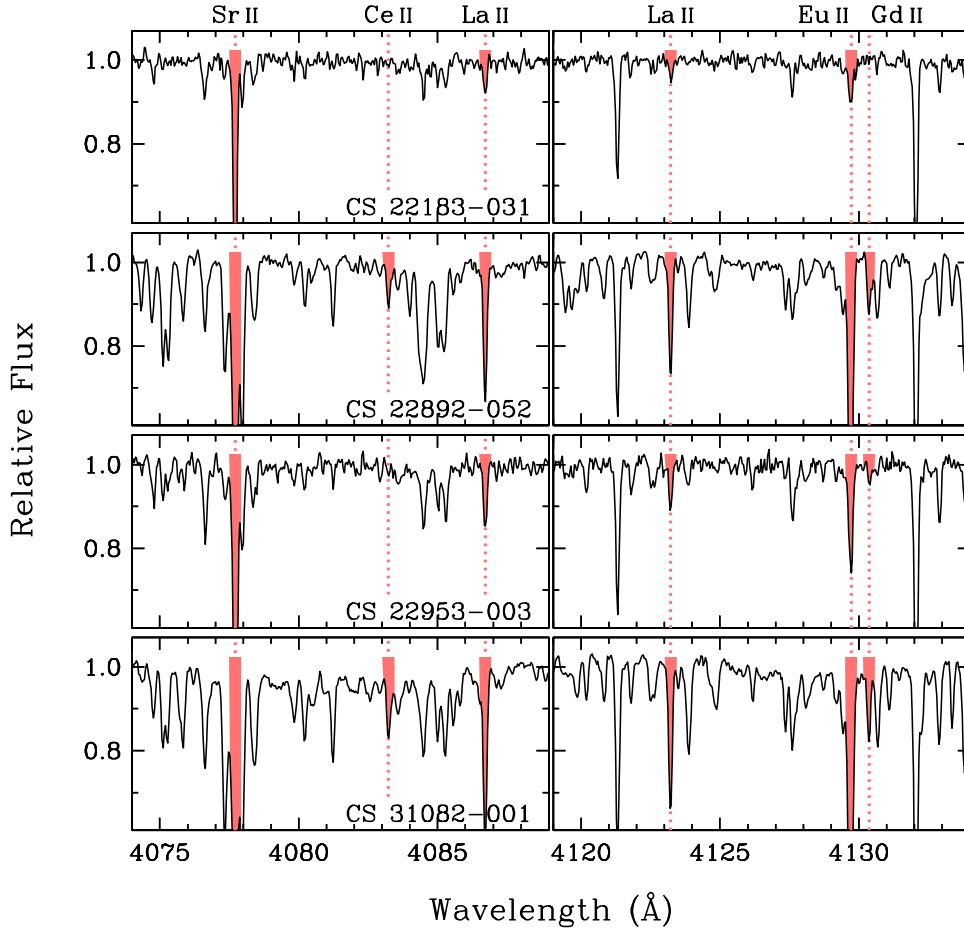


Figure 2. Spectra of the four red giant stars. Shaded regions indicate lines used in the abundance analysis of *n*-capture elements. Species are indicated at the top.

4 COMPARISON WITH PREVIOUS WORK

Table 4 compares the derived stellar parameters and several abundance ratios with those found by previous investigators for the four red giant and three RHB stars in our sample. Most previous studies of red giants calculated T_{eff} using color- T_{eff} relations, frequently leading to warmer T_{eff} and higher metallicity than that found by Roederer et al. (2014a). For the four red giant stars listed in Table 4, our metallicities are lower than those found by previous studies by 0.19 dex ($\sigma = 0.13$). For the RHB stars, our metallicities are lower than those found by previous studies by 0.09 dex ($\sigma = 0.10$). No comparisons are available for the subgiants, but Roederer et al. found that the derived metallicities of 40 subgiants were lower than those found by previous studies by only 0.04 dex ($\sigma = 0.18$).

The [Eu/Fe] ratio is often adopted as a proxy for the overall level of *r*-process enhancement of a star, and our [Eu/Fe] ratios are lower than found by previous studies by 0.22 dex ($\sigma = 0.10$) for the red giants and lower by 0.09 dex ($\sigma = 0.08$) for the stars on the RHB. The reasons for these differences are investigated in detail in Section 9.4 of Roederer et al. In summary, this offset can be explained by the combined effects of different model atmosphere parameters, updates to the analysis code, lines available for analysis, and quality of the observed spectra.

5 RADIAL VELOCITY MEASUREMENTS

Roederer et al. (2014a) measured radial velocities by cross-correlating the spectral order containing the Mg I b lines against metal-poor template standards. Heliocentric corrections were computed using the IRAF *rvcorrect* task. Typical uncertainties are ≈ 0.6 – 0.8 km s $^{-1}$ per observation. Table 1 lists the Heliocentric velocity measurements for each observation.

Repeat observations of CS 22875–029, CS 22882–001, CS 22886–012, CS 22888–047, CS 22892–052, CS 22945–058, and CS 29529–054 show no evidence of radial velocity variations in our data. Preston & Sneden (2001) reported a possible detection of binarity for CS 22892–052, but that preliminary result was based on a tentative phasing of measurements with semi-amplitude of only 1.0 km s $^{-1}$. Subsequent velocity monitoring by our group and others (McWilliam et al. 1995a; Honda et al. 2004a; Bonifacio et al. 2009; Hansen et al. 2011) finds no compelling evidence for velocity variations of CS 22892–052. Comparisons with prior studies of CS 22953–003 (McWilliam et al.; Bonifacio et al.) and CS 31082–001 (Honda et al.; Bonifacio et al.; Hansen et al.) also show no evidence of radial velocity variations. Our measured velocity of CS 22183–031 is 11 km s $^{-1}$ different from two measurements made by Honda et al. (2004a). We are

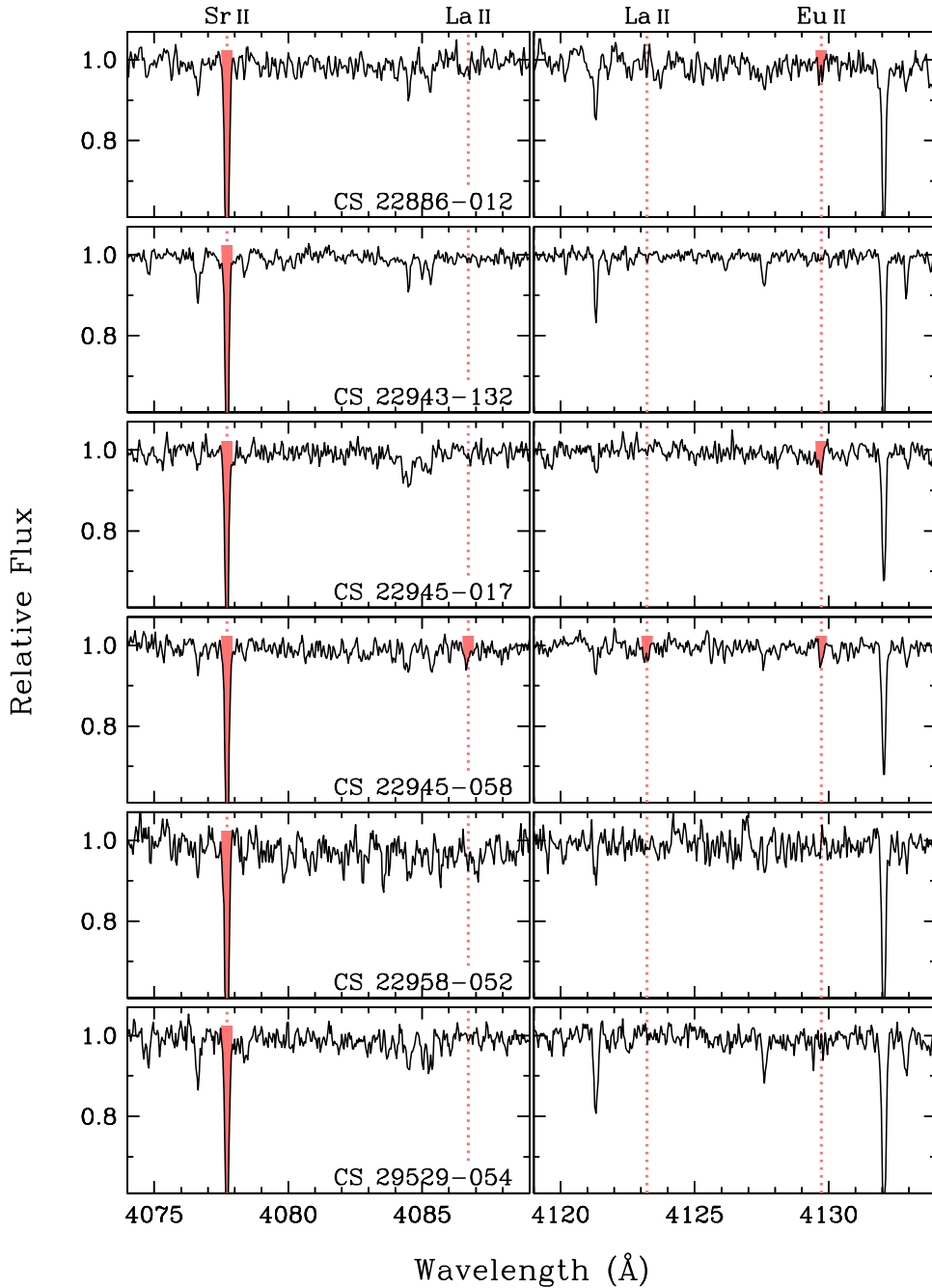


Figure 3. Spectra of the six subgiants. Shaded regions indicate lines used in the abundance analysis of n -capture elements. Species are indicated at the top.

aware of only our single-epoch radial velocity measurements of CS 22943–132, CS 22945–017, and CS 22958–052.

Of the 10 stars in our sample with observations at multiple epochs from all sources, only CS 22183–031 shows compelling evidence for velocity variations. This frequency, 10 per cent, is in reasonable agreement with the 18 per cent binary frequency (3 of 17 stars) of other highly- r -process-enhanced stars reported by Hansen et al. (2011) based on long-term velocity monitoring. Our binary frequency may be underestimated since we have velocity measurements at only two or three epochs for most stars, thus long-period or

low-amplitude binaries may evade our search. In any case, our data support the conclusions of Hansen et al. that there is no evidence to suggest that all highly- r -process-enhanced stars are members of binary or multiple star systems.

6 THE R -PROCESS ABUNDANCE PATTERNS

The heavy element abundance patterns are illustrated in Figures 5, 6, and 7. Three standard abundance templates are shown for comparison. One pattern traces the heavy element abundances in CS 22892–052 as derived by Sneden et al.

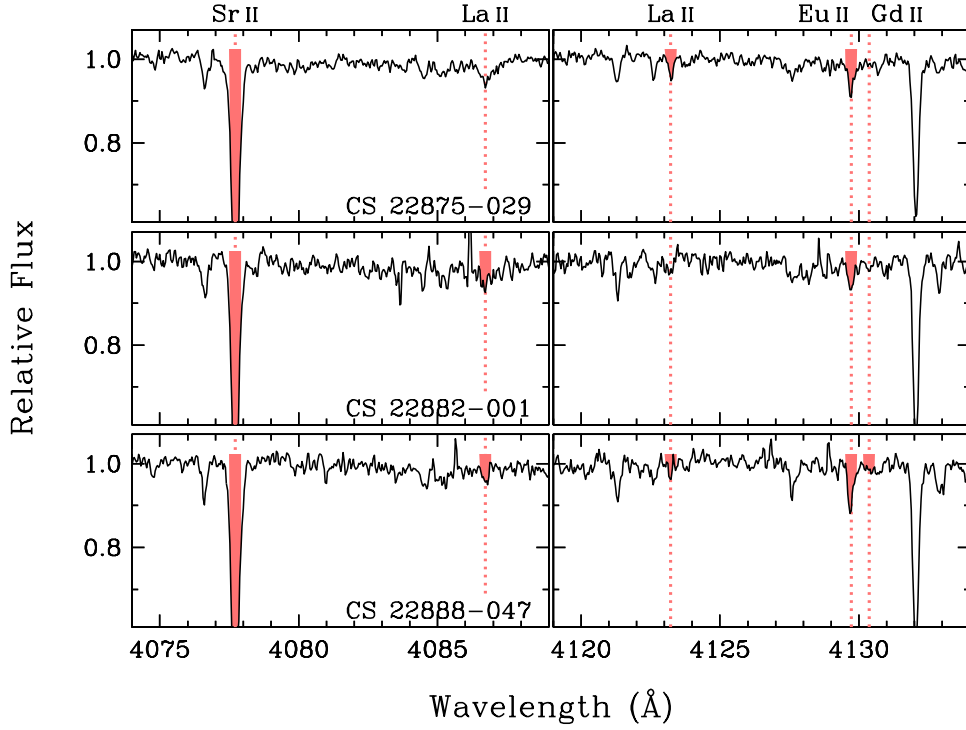


Figure 4. Spectra of the three stars on the RHB. Shaded regions indicate lines used in the abundance analysis of *n*-capture elements. Species are indicated at the top.

Table 3. Atmospheric Parameters and Select Abundance Ratios Sorted by Decreasing [Eu/Fe] Ratios

Star	T_{eff} (K)	$\log g$	v_t (km s $^{-1}$)	[Fe/H] ^a	[Sr/Fe]	[Ba/Fe]	[Eu/Fe]	[Yb/Fe]
Previously-known <i>r</i> -process enhanced stars on the red giant branch								
CS 31082-001	4650 (35)	1.05 (0.14)	1.55 (0.06)	-3.03 (0.07)	+0.67 (0.12)	+0.92 (0.17)	+1.37 (0.16)	+1.38 (0.27)
CS 22892-052	4690 (37)	1.15 (0.15)	1.50 (0.06)	-3.16 (0.07)	+0.68 (0.17)	+0.94 (0.16)	+1.35 (0.22)	+1.39 (0.27)
CS 22183-031	4850 (36)	1.60 (0.14)	1.55 (0.06)	-3.50 (0.07)	-0.22 (0.23)	+0.13 (0.15)	+0.84 (0.16)	+0.68 (0.18)
CS 22953-003	4860 (37)	1.65 (0.17)	1.45 (0.06)	-3.00 (0.07)	+0.32 (0.24)	+0.29 (0.15)	+0.79 (0.15)	+0.63 (0.20)
New <i>r</i> -process enhanced stars on the subgiant branch								
CS 22945-017	6080 (54)	3.70 (0.19)	1.25 (0.06)	-2.73 (0.08)	+0.39 (0.24)	+0.49 (0.14)	+1.13 (0.19)	+1.02 (0.18)
CS 22945-058	5990 (45)	3.65 (0.17)	1.55 (0.06)	-2.71 (0.08)	+0.34 (0.24)	+0.28 (0.14)	+1.13 (0.19)	+0.83 (0.20)
CS 22958-052	6090 (46)	3.75 (0.18)	1.95 (0.06)	-2.42 (0.07)	+0.13 (0.24)	+0.00 (0.15)	+1.00 (0.18)	+0.93 (0.17)
CS 29529-054	5710 (40)	3.55 (0.18)	1.65 (0.06)	-2.75 (0.07)	-0.10 (0.24)	-0.02 (0.15)	+0.90 (0.21)	+0.86 (0.24)
CS 22943-132	5850 (41)	3.60 (0.16)	1.40 (0.06)	-2.67 (0.08)	+0.27 (0.24)	-0.05 (0.14)	+0.86 (0.22)	+0.37 (0.32)
CS 22886-012	5650 (42)	3.50 (0.15)	1.45 (0.06)	-2.61 (0.07)	+0.31 (0.23)	+0.14 (0.14)	+0.85 (0.17)	+0.45 (0.22)
New <i>r</i> -process enhanced stars on the horizontal branch								
CS 22875-029	5990 (44)	1.85 (0.27)	2.80 (0.06)	-2.69 (0.06)	+0.85 (0.22)	+0.30 (0.15)	+0.92 (0.16)	+0.86 (0.19)
CS 22888-047	5950 (46)	1.90 (0.27)	3.00 (0.06)	-2.54 (0.06)	+0.60 (0.22)	+0.04 (0.16)	+0.86 (0.16)	+0.67 (0.18)
CS 22882-001	5930 (52)	1.90 (0.32)	3.00 (0.06)	-2.62 (0.06)	+0.16 (0.25)	+0.06 (0.16)	+0.81 (0.16)	+0.56 (0.19)
Mean ratios for all 13 stars								
...	-2.80 (0.08)	+0.34 (0.09)	+0.27 (0.09)	+0.99 (0.06)	+0.82 (0.09)

^a As derived from Fe II lines

Table 4. Comparison of Derived Model Parameters and Abundances with Previous Work

Star	T_{eff} (K)	$\log g$	v_t (km s^{-1})	[Fe/H] ^a	[Sr/Fe]	[Ba/Fe]	[Eu/Fe]	[Yb/Fe]	Ref.
CS 22183–031 (RG)	4850	1.60	1.55	−3.50	−0.22	+0.13	+0.84	+0.68	1
	5270	2.80	1.20	−2.93	+0.10	+0.38	+1.16	...	2
CS 22892–052 (RG)	4690	1.15	1.50	−3.16	+0.68	+0.94	+1.35	+1.39	1
	4790	1.60	1.80	−2.92	+0.44	+0.92	+1.51	+1.29	2
	4760	1.30	2.29	−3.03	+0.68	+0.93	+1.48	...	3, 4
	4850	1.60	1.90	−3.02	+0.53	+1.01	+1.49	...	5, 6
	4800	1.50	1.95	−3.12	+0.58	+0.92	+1.65	+1.63	7, 8
	4884	1.81	1.67	−2.95	+0.61	+1.19	+1.54	...	9
	4725	1.00	2.00	−3.16	+0.52	+0.89	+1.56	...	10
	4760	1.30	2.30	−3.03	+0.63	+0.89	+1.63	+1.15	11
CS 22953–003 (RG)	4860	1.65	1.45	−3.00	+0.32	+0.29	+0.79	+0.63	1
	4960	1.70	1.95	−2.83	+0.31	+0.00	+0.72	...	3, 4
	5100	2.30	1.70	−2.82	+0.22	+0.49	+1.05	+1.02	5, 6
CS 31082–001 (RG)	4650	1.05	1.55	−3.03	+0.67	+0.92	+1.37	+1.38	1
	4825	1.50	1.80	−2.92	+0.65	+1.17	+1.63	...	12
	4790	1.80	1.90	−2.81	+0.47	+1.02	+1.67	+1.54	2
	4825	1.50	1.80	−2.92	+0.73	+1.16	+1.69	+1.66	13
	4825	1.50	1.80	−2.92	+1.68	+1.57	8
	4922	1.90	1.88	−2.78	+0.53	+1.18	+1.66	...	9
	4925	1.51	1.40	−2.81	+0.66	+1.43	+1.53	...	14
CS 22875–029 (RHB)	5990	1.85	2.80	−2.69	+0.85	+0.30	+0.92	+0.86	1
	6000	2.35	3.05	−2.63	+0.83	+0.48	+1.10	...	15
	6000	2.05	3.00	−2.66	+0.86	+0.44	+0.91	...	16
CS 22882–001 (RHB)	5930	1.90	3.00	−2.62	+0.16	+0.06	+0.81	+0.56	1
	5950	2.50	3.20	−2.45	+0.28	+0.20	+0.92	...	15
	5950	2.00	3.05	−2.54	+0.22	+0.16	+0.84	...	16
CS 22888–047 (RHB)	5950	1.90	3.00	−2.54	+0.60	+0.04	+0.86	+0.67	1
	6000	2.50	3.00	−2.30	+0.63	+0.29	+1.03	...	15
	5850	1.70	3.20	−2.57	+0.31	+0.23	+0.93	...	16
Average differences for the four red giant stars									
Mean	−169	−0.46	−0.33	−0.19	+0.06	−0.11	−0.22	−0.13	
Standard deviation	105	0.35	0.31	0.13	0.13	0.19	0.10	0.22	
No. comparisons	14	14	14	14	15	15	16	7	
Average differences for the three stars on the red horizontal branch									
Mean	−2	−0.30	−0.15	−0.09	+0.02	−0.05	−0.09	...	
Standard deviation	52	0.32	0.10	0.10	0.14	0.15	0.08	...	
No. comparisons	6	6	6	6	6	6	6	...	

Studies that adopted model parameters without change from an earlier study have been excluded from computing the average deviations of T_{eff} , $\log g$, v_t , and [Fe/H].

References: (1) This study; (2) Honda et al. 2004b; (3) McWilliam et al. 1995b; (4) McWilliam 1998; (5) Cayrel et al. 2004; (6) François et al. 2007; (7) Sneden et al. 2003a; (8) Sneden et al. 2009; (9) Barklem et al. 2005; (10) Sneden et al. 1994; (11) Sneden et al. 1996; (12) Hill et al. 2002; (13) Siqueira Mello et al. 2013; (14) Hansen et al. 2012; (15) Preston et al. 2006; (16) For & Sneden 2010

^a As derived from Fe II lines, if specified

(2003a, 2009) and Roederer et al. (2009) from higher quality data. It is reassuring that our derived abundance pattern for CS 22892–052 matches this comparison set so closely. The small deviations for Sr and Ba can be explained by the different microturbulent velocities derived by us (1.50 km s^{-1}) and Sneden et al. (1.95 km s^{-1}), which cause us to derive larger abundances from Sr II and Ba II lines approaching saturation. Another pattern traces the heavy element

abundances in the metal-poor halo star HD 122563, which has normal abundances of the lighter n -capture elements and a deficiency of the heaviest n -capture elements. The pattern found in this star may be considered representative of the so-called weak component of the r -process. The third pattern traces one outcome of s -process nucleosynthesis (Sneden et al. 2008; Bisterzo et al. 2011). In each figure,

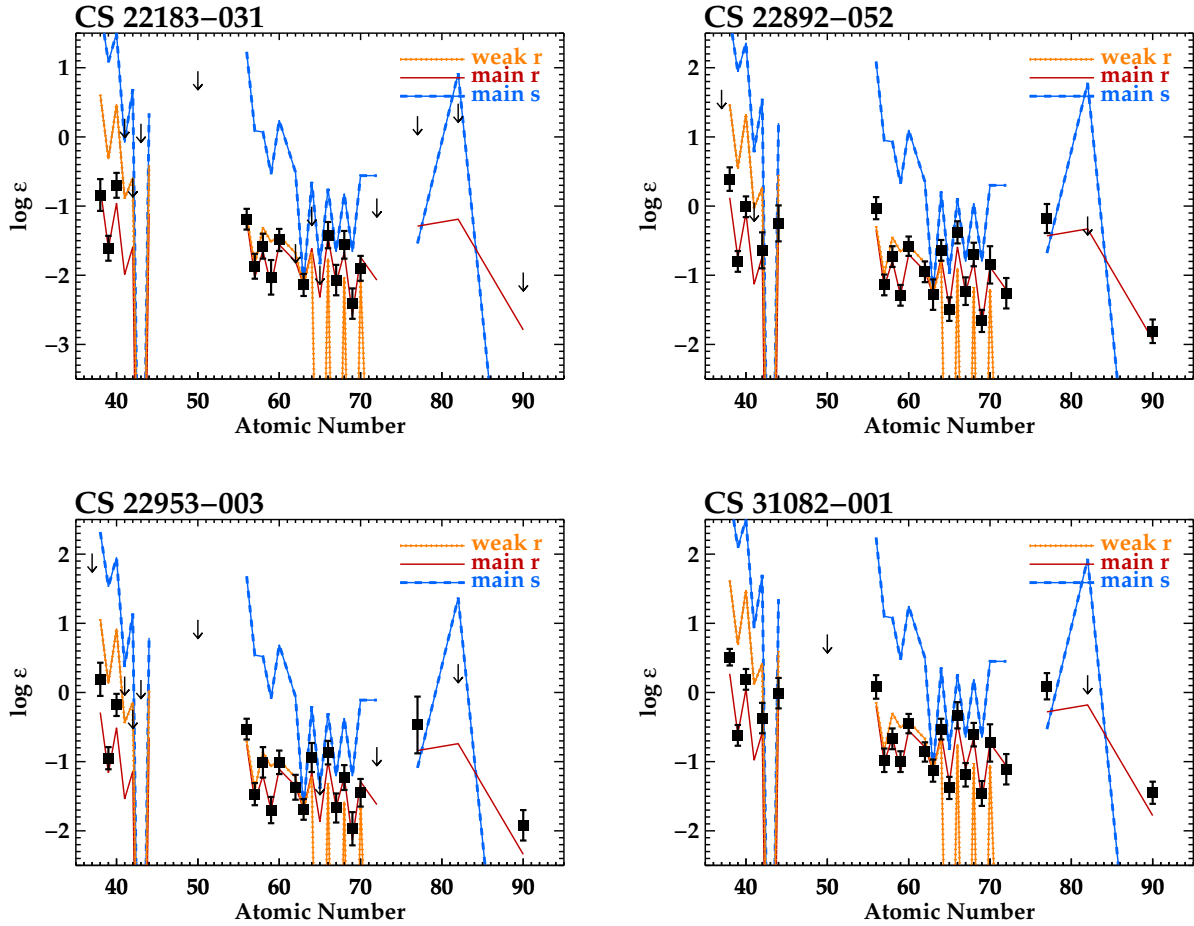


Figure 5. The heavy element distributions in the four red giants: CS 22183–031, CS 22892–052, CS 22953–003, and CS 31082–001. Filled squares mark detections, and arrows mark 3σ upper limits derived from non-detections. The studded orange line marks the scaled heavy element distribution found in the metal-poor giant HD 122563 (Honda et al. 2006; Roederer et al. 2012), frequently referred to as the weak component of the *r*-process. The solid red line marks the scaled heavy element distribution found in CS 22892–052, the main component of the *r*-process, as derived previously by Sneden et al. (2003a, 2009) and Roederer et al. (2009). The long-dashed blue line marks the scaled heavy element distribution predicted by the main and strong components of the *s*-process. Each of the three curves has been renormalized to the Eu abundance.

these patterns are rescaled to match the stellar Eu abundance.

The largest numbers of elements are detected in the red giants, shown in Figure 5. Nearly all of the rare earth elements ($57 \leq Z \leq 71$, plus neighboring elements Ba and Hf) are detected in each case. Ir, a member of the third *r*-process peak, and the actinide Th are also detected in three of these stars. Among the lighter elements, Sr, Y, and Zr are always detectable, and Mo and Ru are detected in two of the stars. Fewer elements are detectable in the subgiants (Figure 6) or field RHB stars (Figure 7). Yet in all of these stars the rare earth elements and those beyond match the pattern in CS 22892–052 established by previous studies.

Only when comparing the ratios of the lighter *n*-capture elements with the rare earth elements do significant differences emerge. This is revealed in Figures 5–7 by the Sr, Y, and Zr abundances that are sometimes enhanced relative to the scaled main component of the *r*-process (solid red line). Numerous studies have pointed out this characteristic in other samples of *r*-process-enhanced field stars, among them McWilliam (1998), Johnson & Bolte (2002), Aoki et al.

(2005), Hansen et al. (2012), and Siqueira-Mello et al. (2014). Curiously, one *r*-process-enhanced metal-poor star analyzed by Roederer et al. (2014c) hints that the so-called universal nature may extend to elements at all three *r*-process peaks (i.e., Se, Te, Os, Pt), regardless of the variations that may occur between the first and second peaks.

We quantify the difference between the lighter and heavier elements in our sample by calculating the dispersions in the [Sr/Ba], [Sr/Eu], [Ba/Eu], and [Eu/Yb] ratios. The [Sr/Ba] and [Sr/Eu] ratios have dispersions of 0.29 and 0.27 dex, respectively. The [Ba/Eu] and [Eu/Yb] ratios, however, have dispersions of only 0.19 and 0.16 dex. The latter two values are consistent with the measurement uncertainties listed in Table 3. This indicates that a real dispersion exists between the lighter and heavier elements, even among members of the class of highly-*r*-process-enhanced stars. The small dispersion in the [Ba/Yb] ratios (0.18 dex) also suggests that the truncated *r*-process (Boyd et al. 2012) did not affect the nucleosynthesis of the heavy elements found in these stars.

In the solar system, approximately 94–98 per cent of

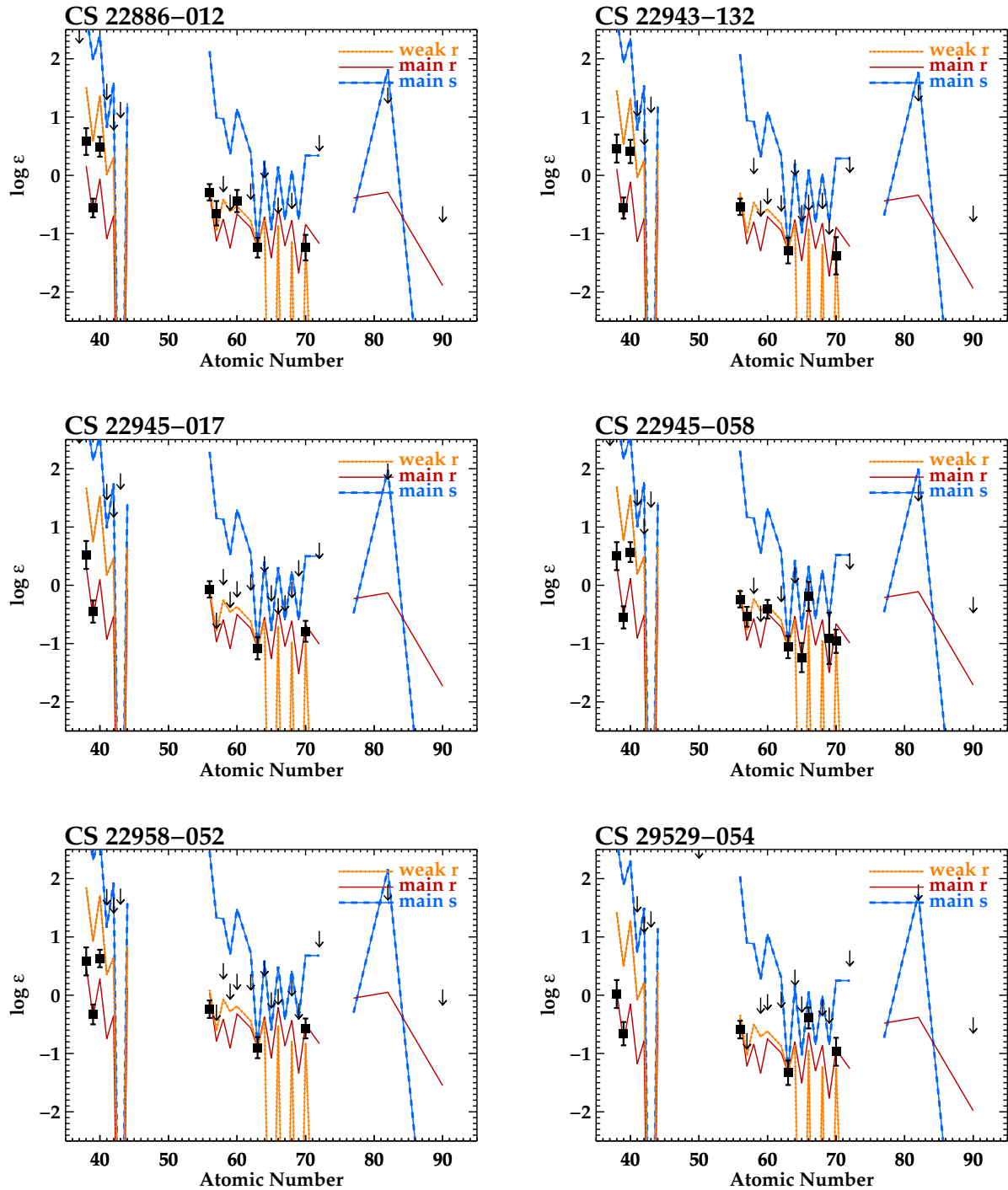


Figure 6. The heavy element distributions in the six subgiants: CS 22886-012, CS 22943-132, CS 22945-017, CS 22945-058, CS 22958-052, and CS 29529-054. Symbols are the same as in Figure 5.

the Eu is predicted to have originated via r -process nucleosynthesis, and the remainder is attributed to s -process nucleosynthesis (e.g., Sneden et al. 2008; Bisterzo et al. 2011). In contrast, only about 11–15 per cent of Ba in the solar system is predicted to have originated via r -process nucleosynthesis. Thus the [Ba/Eu] ratio is commonly used to quantify the relative r - and s -process contributions to a given star or ensemble of stars. The mean [Ba/Eu] ratio for all 13 stars in our sample is -0.71 ± 0.05 ($\sigma = 0.19$). This com-

pares well with other recent estimates by various methods (e.g., -0.70 , Arlandini et al. 1999; -0.81 , Burris et al. 2000; -0.65 , Sneden et al. 2009; -0.78 , Mashonkina & Christlieb 2014).

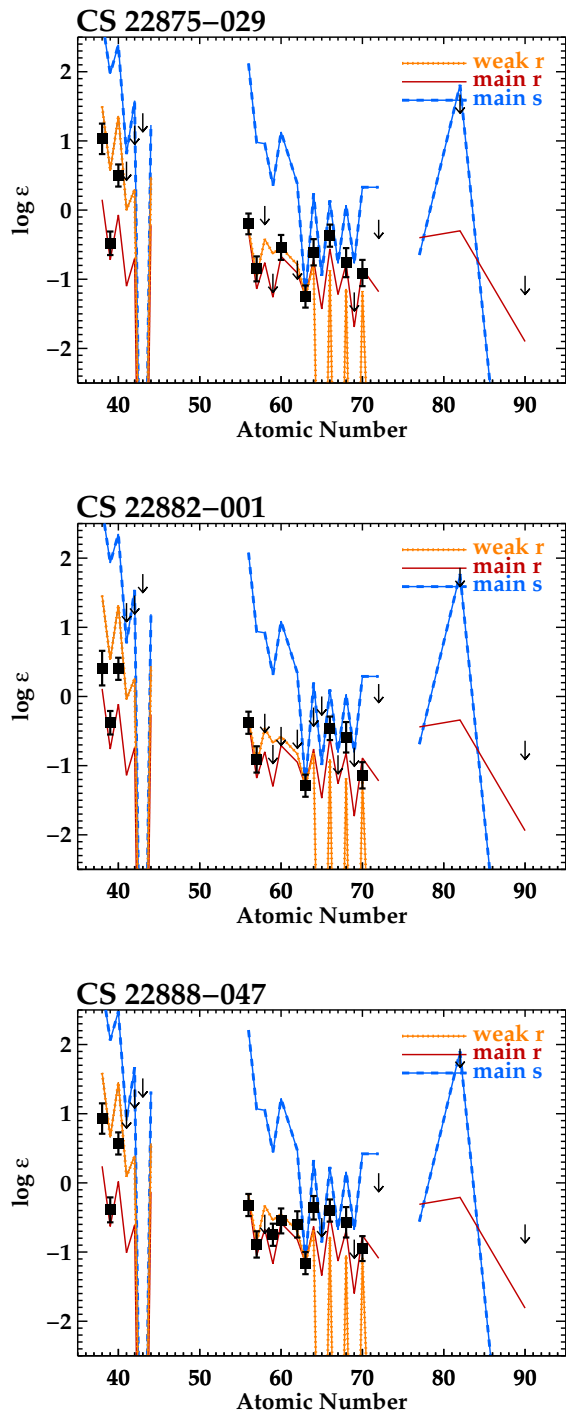


Figure 7. The heavy element distributions in the three stars on the horizontal branch: CS 22875–029, CS 22882–001, and CS 22888–047. Symbols are the same as in Figure 5.

7 STRONGLY *R*-PROCESS ENHANCED STARS ON THE SUBGIANT AND HORIZONTAL BRANCHES

Highly-*r*-process-enhanced stars have now been identified across a broad range of evolutionary states that low-mass stars experience. The first of these such stars identified, CS 22892–052, was a red giant, and for the following 15 years all other members of the class of highly-*r*-process-enhanced

stars identified were also red giants. Aoki et al. (2010) identified the first highly-*r*-process-enhanced star on the main sequence, SDSS J235718.91–005247.8. Our study has identified six new highly-*r*-process-enhanced subgiants and three such RHB stars.

Highly-*r*-process-enhanced subgiants have been found before by the Hamburg/ESO *R*-process Enhanced Star Survey (Barklem et al. 2005), but the stars’ relatively weak lines and the moderate spectral resolution used by Barklem et al. limited their ability to derive abundances of many *n*-capture elements. Preston et al. (2006) also studied the same three RHB stars that we have analyzed, but the focus of that study was not on deriving large numbers of *n*-capture elements to study the abundances patterns in detail.

The unease among practitioners in the field that highly-*r*-process-enhanced stars are found almost exclusively among giants (e.g., Sneden et al. 2008) is put to rest. The bias is observational. Our results and those of Aoki et al. (2010) demonstrate that this phenomenon is not limited to red giants.

8 THE FREQUENCY OF CARBON-ENHANCED METAL-POOR STARS WITH HIGH LEVELS OF *R*-PROCESS ENHANCEMENT

Enhanced [C/Fe] and [N/Fe] ratios were found in the first highly-*r*-process-enhanced star discovered, CS 22892–052 ([C/Fe] = +0.88, [N/Fe] = +1.01; Sneden et al. 1996, 2003a). This raised the question of whether the C- and N-enhancement were related to the *r*-process enhancement. CS 22892–052 is included in our sample.

CS 22945–017 is also highly-enhanced in C and N ([C/Fe] = +1.78, [N/Fe] = +2.05). CS 22943–132 exhibits modest C and N enhancement ([C/Fe] = +0.69, [N/Fe] = +0.49), and C is also modestly enhanced in CS 29529–054 ([C/Fe] = +0.58). All three of these stars are subgiants. Detections of the CH, NH, or CN bands in other highly-*r*-process-enhanced stars indicate that [C/Fe] and [N/Fe] are not enhanced. Four subgiants and all three RHB stars yield only uninteresting upper limits on [N/Fe], but the upper limits derived from the non-detection of CH indicate that [C/Fe] < +1.0 in each of the RHB stars.

The fraction of carbon-enhanced metal-poor stars is known to increase with decreasing metallicity, and these stars typically constitute ≈ 7–32 per cent of local stellar samples with [Fe/H] < –2.0 (Beers et al. 1992; Norris, Ryan, & Beers 1997; Beers & Christlieb 2005; Cohen et al. 2005, 2013; Frebel et al. 2006; Lucatello et al. 2006; Lai et al. 2007; Placco et al. 2011; Carollo et al. 2012, 2014; Lee et al. 2013; Yong et al. 2013). These estimates range by a factor of several because of differing definitions of C enhancement, metallicity ranges considered, sample sizes and selection techniques, and median distance from the sun. Some of these stars are found in binary systems and presumably acquired their C enhancement through mass transfer from a more evolved companion. Long-term velocity monitoring and detailed studies of the *n*-capture abundance patterns indicate that this explanation cannot be applied to other carbon-enhanced metal-poor stars (e.g., Aoki et al. 2002, Ryan et al. 2005, Roederer et al. 2014b).

In our sample of highly- r -process-enhanced stars, finding 2 of 13 stars as carbon-enhanced (15 per cent) is consistent with previous estimates. There is no compelling reason to suspect that the r -process and C-enhancement are related.

9 LIGHT-ELEMENT ABUNDANCE SIGNATURES RELATED TO HIGH LEVELS OF R -PROCESS ENHANCEMENT

The large, homogeneous dataset of Roederer et al. (2014a) affords a unique opportunity to compare abundances in individual stars to abundances in large samples of stars with similar stellar parameters. These comparisons will be minimally affected by uncertainties in the stellar parameters, non-LTE effects, poorly-known atomic data, etc. Subtle but significant outlying abundance ratios may be identified this way. We use this technique to identify any abundance signatures among the light elements, those with $6 \leq Z \leq 30$, that are peculiar to the highly- r -process-enhanced stars relative to normal metal-poor stars. Any peculiar abundance signatures found could be associated with the supernovae or other sites capable of generating large amounts of elements beyond the second r -process peak.

We perform this test for each of the 13 stars in our sample. We begin by identifying a comparison sample of stars for each r -process-enhanced star that are in the same evolutionary state, have T_{eff} within ± 200 K, and are within ± 0.3 dex of the metallicity of the r -process-enhanced star. We exclude other highly- r -process-enhanced stars from the comparison samples. We also exclude stars whose heavy elements indicate the presence of a large amount of s -process material, since the present-day composition of these stars may not accurately reflect the composition of their birth clouds. The comparison samples typically include 20–30 stars from Roederer et al. (2014a), but there as many as 61 stars or as few as 6 stars for comparison in some cases.

Figures 8–10 illustrate the $[X/\text{Fe}]$ ratios for each r -process enhanced star. The mean $\pm 1\sigma$ standard deviation of each $[X/\text{Fe}]$ ratio for the comparison sample is marked by the shaded box. The number of comparison stars is indicated in each figure caption. These figures illustrate that the light-element abundance ratios of highly- r -process-enhanced stars rarely deviate by more than 1σ from those of other metal-poor stars. Like other metal-poor stars, the highly- r -process-enhanced stars show $[\alpha/\text{Fe}]$ ratios (where α indicates O, Mg, Si, Ca, and Ti) enhanced by factors of a few relative to the solar ratios. The iron-group elements are typically found in solar or sub-solar ratios in both the r -process enhanced stars and the normal metal-poor stars. By construction, the n -capture elements Sr, Y, Zr, Ba, and Eu are significantly enhanced relative to the comparison stars.

Finally, we illustrate the mean deviations of each star from its comparison sample in Figure 11. These values are listed in Table 5. The points in Figure 11 represent an unweighted mean of $[X/\text{Fe}]_i - \langle [X/\text{Fe}] \rangle$ calculated for each element X in each r -process enhanced star. The error bars in Figure 11 represent the standard deviation of the mean. When multiple ionization states of an element are detected, each ionization state is considered separately. Species are only illustrated in Figure 11 when the mean of the differ-

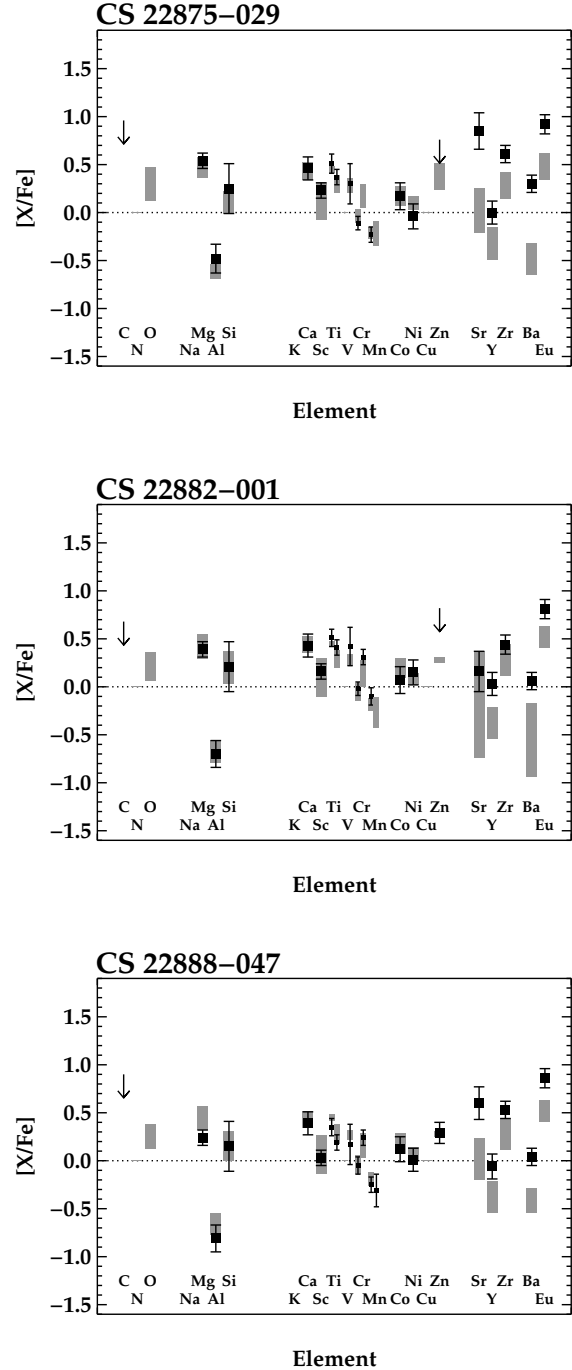


Figure 10. Comparison of abundances in the r -process enhanced stars on the horizontal branch with the average abundances of other stars with T_{eff} within ± 200 K and $[\text{Fe}/\text{H}]$ within ± 0.3 dex of each. For CS 22875-029, CS 22882-001, and CS 22888-047, the numbers of stars in the comparison samples are eight, seven, and six, respectively. Symbols are the same as in Figure 8.

ences has been computed from more than three stars. None of the differences illustrated in Figure 11 is significant at the 2σ level or greater, and most light-element ratios in r -process enhanced stars are consistent with the comparison samples at the 1σ level. The mean of the absolute values of these differences for 15 $[X/\text{Fe}]$ ratios from Mg to Zn is 0.015 ± 0.008 dex ($\sigma = 0.030$ dex), or 3.5 per cent.

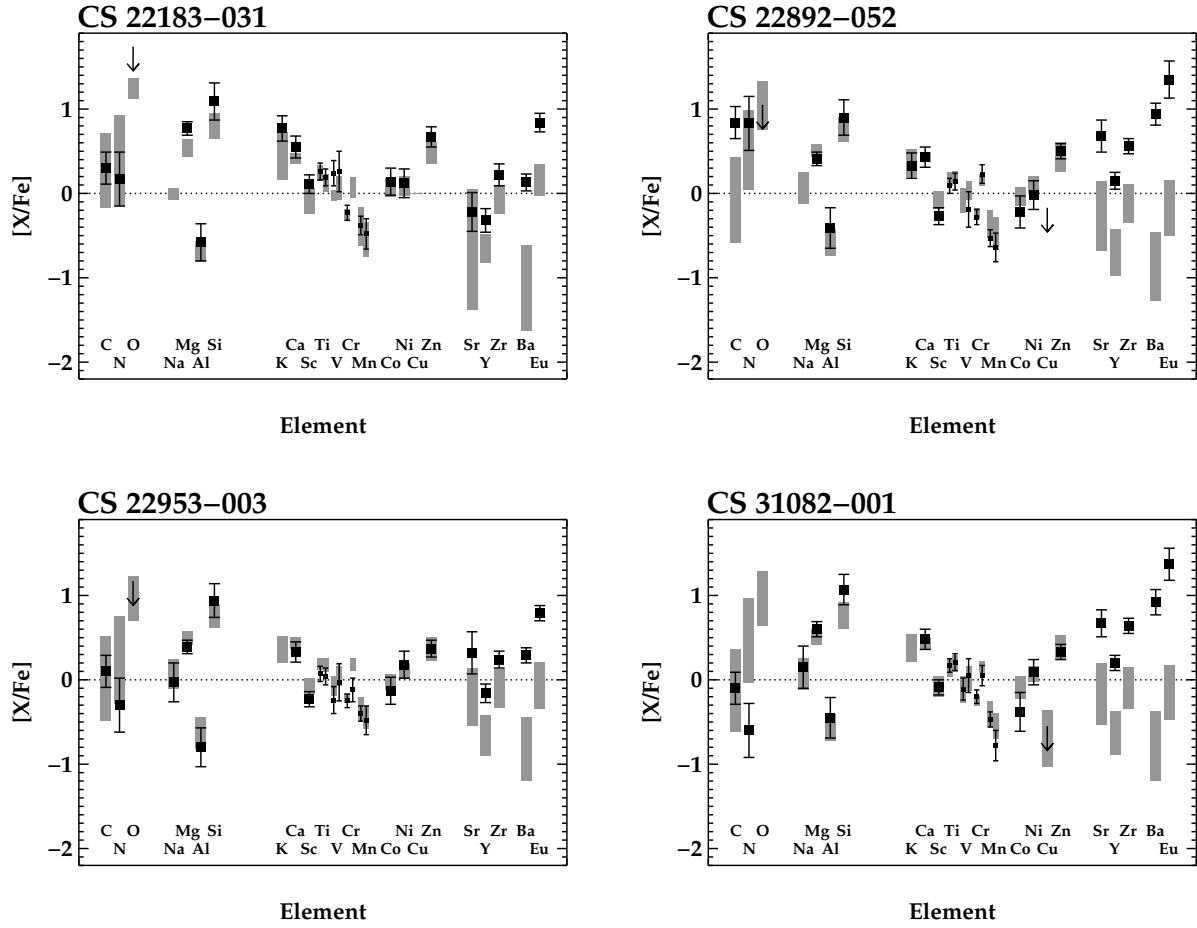


Figure 8. Comparison of abundances in the *r*-process enhanced red giants with the average abundances of other stars with T_{eff} within ± 200 K and $[\text{Fe}/\text{H}]$ within ± 0.3 dex of each. For CS 22183–031, CS 22892–052, CS 22953–003, and CS 31082–001, the numbers of stars in the comparison samples are 12, 23, 30, and 23, respectively. The comparison sample is shown by the shaded gray boxes, representing the mean $\pm 1\sigma$ standard deviations. The comparison sample is only shown if it is derived from three or more stars. Smaller symbols are shown for Ti, V, Cr, and Mn to accommodate ratios from both the neutral and ionized states, which may differ. The dotted line marks the solar ratios.

In summary, we find no compelling evidence that any of the light-element ratios are significantly different in the highly-*r*-process-enhanced stars and metal-poor stars without high levels of *r*-process enhancement. This complements results derived from a sample of seven moderately-*r*-process-enhanced stars (Siqueira-Mello et al. 2014). That study found no difference between the $[\text{X}/\text{Fe}]$ ratios (where X represents any of 13 elements between Mg and Ni) among the *r*-process-enhanced and unenhanced groups of stars.

We conclude that the nucleosynthetic sites responsible for producing the large *r*-process enhancement did not produce any detectable light-element abundance signatures unique from the core-collapse supernovae widely believed to have produced the metals observed in the vast majority of metal-poor stars. This scenario may come about naturally by decoupling the sites of large *r*-process enhancement from core-collapse supernovae entirely; e.g., if mergers of neutron stars are the source of this kind of *r*-process enhancement. Alternatively, if development of the conditions required for this kind of *r*-process nucleosynthesis is effectively decoupled from the deep regions of supernovae where light-element production occurs, this would also satisfy the observations.

Table 5. Mean differences between *r*-process-enhanced stars and comparison samples

Ratio	$\langle\Delta\rangle$	std. dev.	std. err.	N_{stars}
[C/Fe]	+0.322	0.52	0.17	9
[N/Fe]	+0.172	1.08	0.44	6
[Mg I/Fe]	-0.003	0.12	0.03	13
[Al I/Fe]	+0.052	0.12	0.03	13
[Si I/Fe]	+0.103	0.18	0.05	11
[Ca I/Fe]	+0.005	0.07	0.02	13
[Sc II/Fe]	+0.027	0.12	0.03	13
[Ti I/Fe]	-0.021	0.12	0.03	13
[Ti II/Fe]	-0.010	0.08	0.02	13
[V II/Fe]	+0.034	0.14	0.05	9
[Cr I/Fe]	-0.007	0.04	0.01	13
[Cr II/Fe]	-0.027	0.17	0.06	7
[Mn I/Fe]	+0.000	0.10	0.03	13
[Mn II/Fe]	-0.051	0.13	0.05	6
[Co I/Fe]	-0.042	0.11	0.03	13
[Ni I/Fe]	-0.006	0.08	0.02	12
[Zn I/Fe]	+0.021	0.27	0.10	7

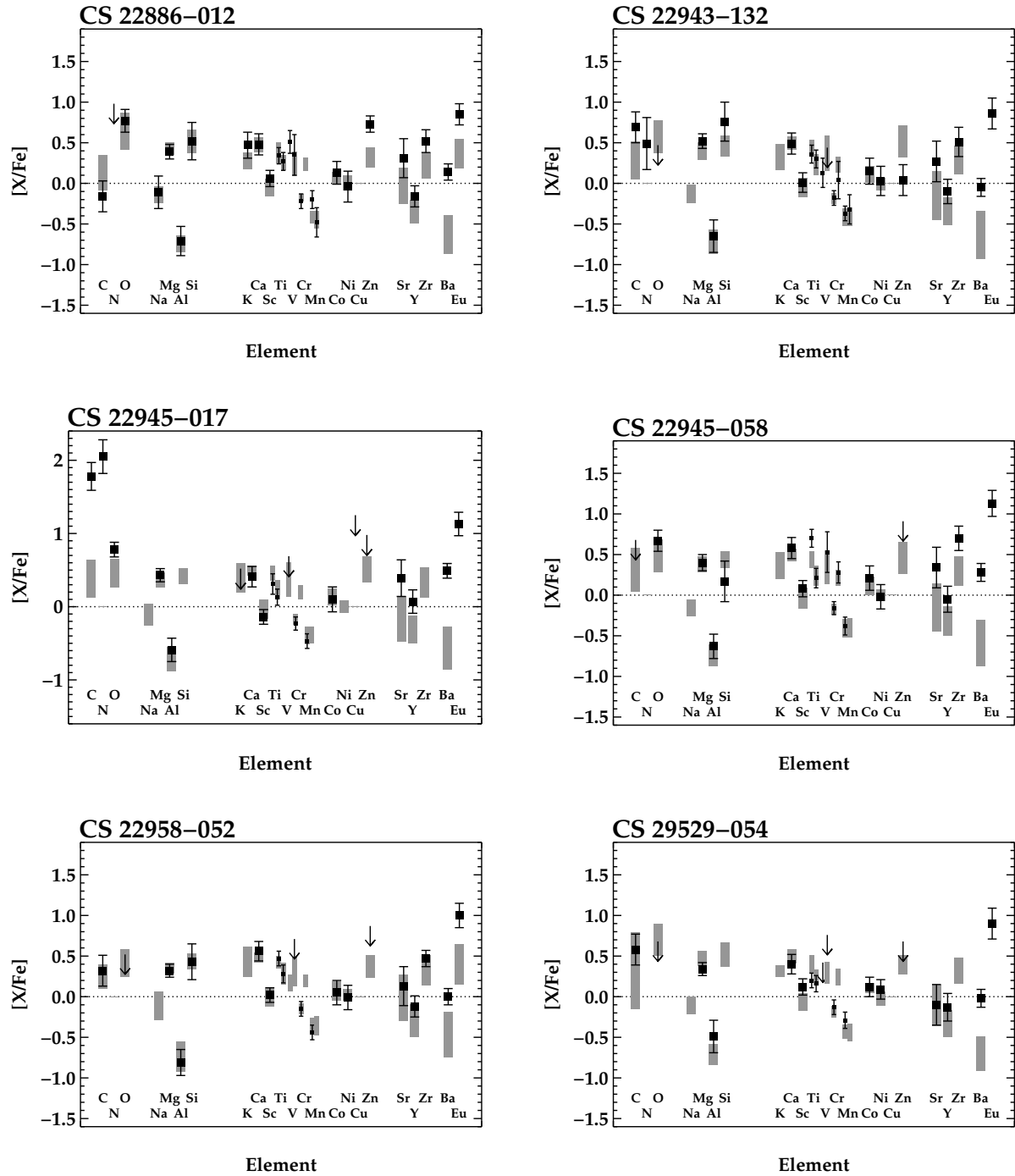


Figure 9. Comparison of abundances in the r -process enhanced subgiants with the average abundances of other stars with T_{eff} within ± 200 K and $[\text{Fe}/\text{H}]$ within ± 0.3 dex of each. For CS 22886-012, CS 22943-132, CS 22945-017, CS 22945-058, CS 22958-052, and CS 29529-054, the numbers of stars in the comparison samples are 20, 50, 52, 61, 38, and 23, respectively. Symbols are the same as in Figure 8.

A decoupling between light-element and r -process nucleosynthesis has been proposed previously (e.g., Wasserburg & Qian 2000; Fields, Truran, & Cowan 2002) to satisfy the observed dispersion of $[\text{Eu}/\text{Fe}]$ ratios at low metallicity compared to, e.g., the $[\text{Mg}/\text{Fe}]$ ratios, as illustrated in Figure 14 of Sneden et al. (2008). Our results reaffirm this situation, extend it to other elements, and con-

strain the amount of variation allowed in the individual light-element yields.

10 SUMMARY

We have examined the abundance patterns found in stars with high levels of r -process enrichment as indicated by

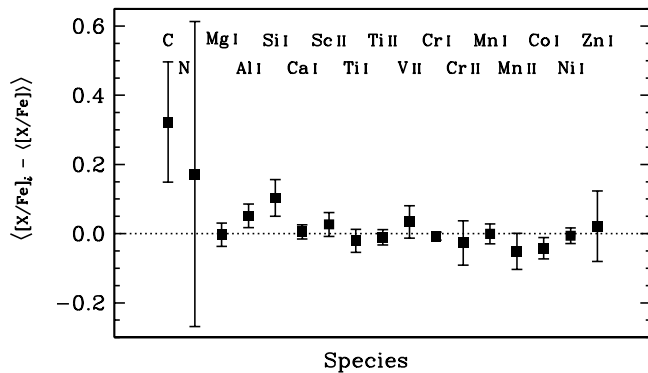


Figure 11. Mean residuals between each $[X/Fe]$ ratio in each star and its comparison sample. The uncertainties correspond to the standard deviation of the mean. Only comparisons between more than three stars are illustrated. None of the mean residuals is significant at the 2σ level.

their enhanced $[Eu/Fe]$ ratios. Our study differs from the *r*-process survey of Barklem et al. (2005) by deriving abundances from higher-resolution spectra that cover a wider wavelength range. Thirteen of the 313 metal-poor stars analyzed by Roederer et al. (2014a) are identified as members of the class of *r*-II stars after correcting for offsets in the derived $[Eu/Fe]$ ratios ($[Eu/Fe] \gtrsim +0.8$). Four of these stars are red giants whose high levels of *r*-process enhancement were known previously. We identify six new subgiants (including the MSTO phase) and three new RHB members of this class. Aoki et al. (2010) also identified one such star on the main sequence. Once limited to the realm of red giants, highly-*r*-process-enhanced stars are now known all across a broad range of stellar evolutionary states.

The first highly-*r*-process-enhanced star discovered, CS 22892-052, was also enhanced in C and N, which signaled a possible connection between these chemical signatures. Only 2 of the 13 stars in our sample (including CS 22892-052) are enhanced in C and N, however, offering no compelling evidence for such a connection. We also find no compelling evidence to suggest that a disproportionately high fraction of highly-*r*-process-enhanced stars are members of binary or multiple star systems, confirming the conclusions of a dedicated radial velocity survey by Hansen et al. (2011). The dispersion in the $[Sr/Ba]$ and $[Sr/Eu]$ ratios is larger than the dispersion in the $[Ba/Eu]$ or $[Yb/Eu]$ ratios, indicating that the robust pattern does not extend to the elements between the first and second *r*-process peaks even within the class of highly-*r*-process-enhanced stars.

We compare the light-element ($Z \leq 30$) abundance pattern in each highly-*r*-process-enhanced star with the light-element abundance pattern in a comparison set of stars that have similar stellar parameters but lack high levels of *r*-process enhancement. This test reveals no obvious light-element abundance signatures that are unique to the highly-*r*-process-enhanced stars. The nucleosynthetic sites responsible for producing the large *r*-process enhancement apparently did not produce any detectable light-element abundance signatures distinct from normal core-collapse supernovae responsible for much of the early metal production in the universe.

ACKNOWLEDGMENTS

We thank the referee, T. Beers, for a prompt and helpful report. This research has made use of NASA's Astrophysics Data System Bibliographic Services, the arXiv preprint server operated by Cornell University, the SIMBAD and VizieR databases hosted by the Strasbourg Astronomical Data Center, and the Atomic Spectra Database hosted by the National Institute of Standards and Technology. IRAF is distributed by the National Optical Astronomy Observatories, which are operated by the Association of Universities for Research in Astronomy, Inc., under cooperative agreement with the National Science Foundation. C. S. is supported by the U.S. National Science Foundation (grant AST 12-11585).

REFERENCES

- Aoki W., Norris J. E., Ryan S. G., Beers T. C., Ando H. 2002, *ApJ*, 567, 1166
Aoki W. et al. 2005, *ApJ*, 632, 611
Aoki W., Beers T. C., Honda S., Carollo D. 2010, *ApJL*, 723, L201
Aoki W., Suda T., Boyd R. N., Kajino T., Famiano M. A. 2013, *ApJL*, 766, L13
Arlandini C., Käppeler F., Wisshak K., Gallino R., Lugaro M., Busso M., Straniero O. 1999, *ApJ*, 525, 886
Asplund M., Grevesse N., Sauval A. J., Scott P. 2009, *ARA&A*, 47, 481
Barklem P. S. et al. 2005, *A&A*, 439, 129
Beers T. C., Preston G. W., Shectman S. A. 1992, *AJ*, 103, 1987
Beers T. C., Christlieb N. 2005, *ARA&A*, 43, 531
Bernstein R., Shectman S. A., Gunnels S. M., Mochnacki S., Athey A. E. 2003, *Proc. SPIE*, 4841, 1694
Bisterzo S., Gallino R., Straniero O., Cristallo S., Käppeler F. 2011, *MNRAS*, 418, 284
Bonifacio P. et al. 2009, *A&A*, 501, 519
Boyd R. N., Famiano M. A., Meyer B. S., Motizuki Y., Kajino T., Roederer I. U. 2012, *ApJL*, 744, L14
Burbidge E. M., Burbidge G. R., Fowler W. A., Hoyle F. 1957, *Rev. Mod. Phys.*, 29, 547
Burriss D. L., Pilachowski C. A., Armandroff T. E., Sneden C., Cowan J. J., Roe H. 2000, *ApJ*, 544, 302
Cameron A. G. W. 1973, *Space Sci. Rev.*, 15, 121
Carollo D. et al. 2012, *ApJ*, 744, 195
Carollo D., Freeman K., Beers T. C., Placco V. M., Tumlinson J., Martell S. L. 2014, *ApJ*, 788, 180
Cayrel R. et al. 2004, *A&A*, 416, 1117
Cescutti G., Chiappini C., Hirschi R., Meynet G., Frischknecht U. 2013, *A&A*, 553, A51
Christlieb N., Schörck T., Frebel A., Beers T. C., Wistozki L., Reimers D. 2008, *A&A*, 484, 721
Cohen J. G. et al. 2005, *ApJL*, 633, L109
Cohen J., Christlieb N., Thompson I., McWilliam A., Shectman S., Reimers D., Wistozki L., Kirby E. 2013, *ApJ*, 778, 56
Cowan J. J., Burriss D. L., Sneden C., McWilliam A., Preston G. W. 1995, *ApJL*, 439, L51
Cowan J. J. et al. 2002, *ApJ*, 572, 861
Cowan J. J., Roederer I. U., Sneden C., Lawler J. E. 2011, *RR Lyrae Stars, Metal-Poor Stars, and the Galaxy*, 223

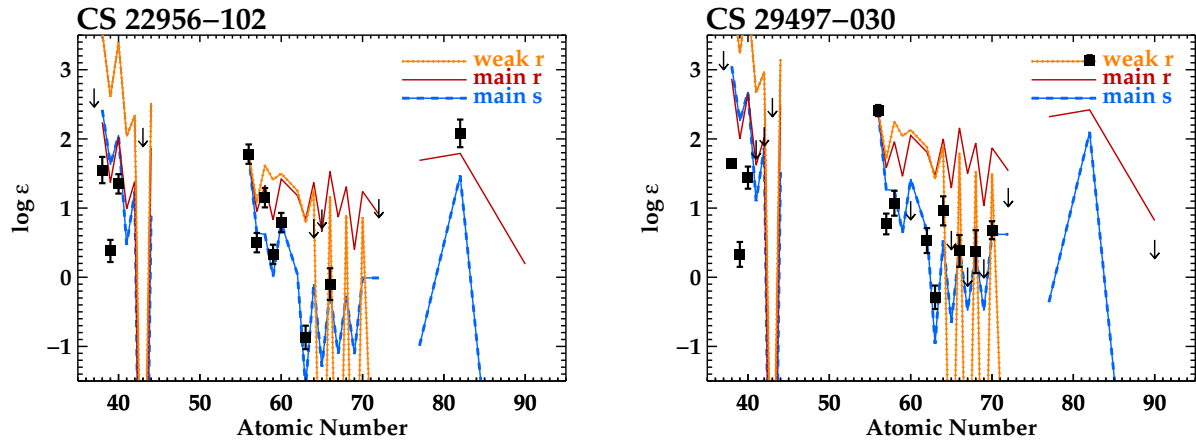


Figure 12. The heavy element distributions in CS 22956–102 and CS 29497–030. Symbols are the same as in Figure 5. The curves have been normalized to the Ba abundance in each star.

- Demarque P., Woo J.-H., Kim Y.-C., Yi S. K. 2004, *ApJS*, 155, 667
- Fabbian D., Asplund M., Barklem P. S., Carlsson M., Kiselman D. 2009, *A&A*, 500, 1221
- Fields B. D., Truran J. W., Cowan J. J. 2002, *ApJ*, 575, 845
- For B.-Q., Sneden C. 2010, *AJ*, 140, 1694
- François P. et al. 2007, *A&A*, 476, 935
- Frebel A. et al. 2006, *ApJ*, 652, 1585
- Gallino R., Arlandini C., Busso M., Lugaro M., Travaglio C., Straniero O., Chieffi A., Limongi M. 1998, *ApJ*, 497, 388
- Gustafsson B., Edvardsson B., Eriksson K., Jørgensen U. G., Nordlund Å., Plez B. 2008, *A&A*, 486, 951
- Hansen T., Andersen J., Nordström B., Buchhave L. A., Beers T. C. 2011, *ApJL*, 743, L1
- Hansen C. J. et al. 2012, *A&A*, 545, A31
- Hill V. et al. 2002, *A&A*, 387, 560
- Honda S. et al. 2004a, *ApJS*, 152, 113
- Honda S., Aoki W., Kajino T., Ando H., Beers T. C., Izumiura H., Sadakane K., Takada-Hidai M. 2004b, *ApJ*, 607, 474
- Honda S., Aoki W., Ishimaru Y., Wanajo S., Ryan S. G. 2006, *ApJ*, 643, 1180
- Ivans I. I., Sneden C., Gallino R., Cowan J. J., Preston G. W. 2005, *ApJL*, 627, L145
- Johnson J. A., Bolte M. 2002, *ApJ*, 579, 616
- Kelson D. D. 2003, *PASP*, 115, 688
- Kratz K.-L., Farouqi K., Pfeiffer B., Truran J. W., Sneden C., Cowan J. J. 2007, *ApJ*, 662, 39
- Kurucz R. L., Bell B. 1995, *Kurucz CD-ROM*, Cambridge, MA: Smithsonian Astrophysical Observatory
- Lai D. K., Johnson J. A., Bolte M., Lucatello S. 2007, *ApJ*, 667, 1185
- Lee Y. S., et al. 2013, *AJ*, 146, 132
- Lind K., Asplund M., Barklem P. S. 2009, *A&A*, 503, 541
- Lind K., Asplund M., Barklem P. S., Belyaev A. K. 2011, *A&A*, 528, A103
- Lucatello S., Beers T. C., Christlieb N., Barklem P. S., Rossi S., Marsteller B., Sivarani T., Lee Y. S. 2006, *ApJL*, 652, L37
- Mashonkina L. Christlieb N. 2014, *A&A*, 565, A123
- McWilliam A., Preston G. W., Sneden C., Shtetman S. 1995a, *AJ*, 109, 2736
- McWilliam A., Preston G. W., Sneden C., Searle L. 1995b, *AJ*, 109, 2757
- McWilliam A. 1998, *AJ*, 115, 1640
- Montes F. et al. 2007, *ApJ*, 671, 1685
- Norris J. E., Ryan S. G., Beers T. C. 1997, *ApJ*, 488, 350
- Placco V. M. et al. 2011, *AJ*, 142, 188
- Preston G. W., Sneden C. 2000, *AJ*, 120, 1014
- Preston G. W., Sneden C. 2001, *AJ*, 122, 1545
- Preston G. W., Sneden C., Thompson I. B., Shtetman S. A., Burley G. S. 2006, *AJ*, 132, 85
- Qian Y.-Z., Wasserburg G. J. 2008, *ApJ*, 687, 272
- Roederer I. U., Kratz K.-L., Frebel A., Christlieb N., Pfeiffer B., Cowan J. J., Sneden C. 2009, *ApJ*, 698, 1963
- Roederer I. U., Cowan J. J., Karakas A. I., Kratz K.-L., Lugaro M., Simmerer J., Farouqi K., Sneden C. 2010, *ApJ*, 724, 975
- Roederer I. U. et al. 2012, *ApJS*, 203, 27
- Roederer I. U. 2013, *AJ*, 145, 26
- Roederer I. U., Preston G. W., Thompson I. B., Shtetman S. A., Sneden C., Burley G. S., Kelson D. 2014a, *AJ*, 147, 136
- Roederer I. U., Preston G. W., Thompson I. B., Shtetman S. A., Sneden C. 2014b, *ApJ*, 784, 158
- Roederer I. U. et al. 2014c, *ApJ*, 791, 32
- Rossi S., Beers T. C., Sneden C., Sevastyanenko T., Rhee J., Marsteller B. 2005, *AJ*, 130, 2804
- Ryan S. G., Aoki W., Norris J. E., Beers T. C. 2005, *ApJ*, 635, 349
- Siqueira Mello C. et al. 2013, *A&A*, 550, A122
- Siqueira-Mello C. et al. 2014, *A&A*, 565, A93
- Sneden C. A. 1973, Ph.D. Thesis, Univ. of Texas at Austin
- Sneden C., Parthasarathy M. 1983, *ApJ*, 267, 757
- Sneden C., Preston G. W., McWilliam A., Searle L. 1994, *ApJL*, 431, L27
- Sneden C., McWilliam A., Preston G. W., Cowan J. J., Burris D. L., Armosky B. J. 1996, *ApJ*, 467, 819
- Sneden C. et al. 2003a, *ApJ*, 591, 936
- Sneden C., Preston G. W., Cowan J. J. 2003, *ApJ*, 592, 504
- Sneden C., Cowan J. J., Gallino R. 2008, *ARA&A*, 46, 241

- Sneden C., Lawler J. E., Cowan J. J., Ivans I. I., Den Hartog E. A. 2009, *ApJS*, 182, 80
 Sobeck J. S. et al. 2011, *AJ*, 141, 175
 Takeda Y., Zhao G., Chen Y.-Q., Qiu H.-M., Takada-Hidai M. 2002, *PASJ*, 54, 275
 Truran J. W., Cowan J. J., Pilachowski C. A., Sneden C. 2002, *PASP*, 114, 1293
 Wallerstein G., Greenstein J. L., Parker R., Helfer H. L., Aller L. H. 1963, *ApJ*, 137, 280
 Wasserburg G. J., Qian Y.-Z. 2000, *ApJL*, 529, L21
 Westin J., Sneden C., Gustafsson B., Cowan J. J. 2000, *ApJ*, 530, 783
 Yong D. et al. 2013, *ApJ*, 762, 26

APPENDIX A: TWO STARS WITH EUROPIUM ENHANCEMENTS FROM *S*-PROCESS NUCLEOSYNTHESIS

CS 29497–030 has been identified previously using traditional signatures of *s*-process enrichment from a binary companion that passed through the thermally-pulsing asymptotic giant branch (TP-AGB) phase of evolution: radial velocity variations, a strong CH G band indicating substantial C enhancement, and an *n*-capture abundance pattern indicative of *s*-process enhancement (Preston & Sneden 2000; Sneden, Preston, & Cowan 2003; Ivans et al. 2005). Roederer et al. (2014a) derived $[C/Fe] = +2.38$, $[Ba/Fe] = +2.75$, $[Eu/Fe] = +1.70$, and $[Pb/Fe] = +3.62$ for CS 29497–030. The *n*-capture abundance pattern of CS 29497–030 is illustrated in Figure 12. Relative to the template *s*-process pattern shown for comparison, elements at the first *s*-process peak ($38 \leq Z \leq 40$) are underabundant and lead ($Z = 82$) is overabundant. This is explained by the high neutron-to-seed ratio found in low-mass TP-AGB stars at low metallicity (e.g., Gallino et al. 1998).

CS 22956–102 also exhibits similar characteristics, as well as a weak but detectable C₂ band-head near 5165 Å. Rossi et al. (2005) identified CS 22956–102 as a carbon-enhanced metal-poor star, but Roederer et al. (2014a) published the first detailed abundance pattern derived from high resolution spectroscopic observations. Roederer et al. also uncovered evidence of radial velocity variations for this star. Roederer et al. derived $[C/Fe] = +2.03$, $[Ba/Fe] = +1.81$, $[Eu/Fe] = +0.82$, and $[Pb/Fe] = +2.43$ for CS 22956–102. The *n*-capture abundance pattern of CS 22956–102 is also illustrated in Figure 12. Each of these stars exhibits unmistakable evidence that the high levels of Eu enhancement observed cannot be mainly attributed to *r*-process nucleosynthesis.